# Synthesis, physical properties, and band structure of the layered bismuthide $PtBi_2$

C. Q. Xu,[1,2] X. Z. Xing,[3] Xiaofeng Xu,[1,2,*] Bin Li,[4,†] B. Chen,[5] L. Q. Che,[6] Xin Lu,[6] Jianhui Dai,[1] and Z. X. Shi[3]

[1]*Department of Physics and Hangzhou Key Laboratory of Quantum Matters, Hangzhou Normal University, Hangzhou 310036, China*

[2]*Department of Physics, Changshu Institute of Technology, Changshu 215500, China*

[3]*Department of Physics and Key Laboratory of MEMS of the Ministry of Education, Southeast University, Nanjing 211189, China*

[4]*Information Physics Research Center, Nanjing University of Posts and Telecommunications, Nanjing 210023, China*

[5]*Department of Physics, University of Shanghai for Science & Technology, Shanghai 200093, China*

[6]*Center for Correlated Matter and Department of Physics, Zhejiang University, Hangzhou 310058, China*

(Received 3 July 2016; published 10 October 2016)

We report details of single-crystal growth of stoichiometric bismuthide $PtBi_2$ whose structure consists of alternate stacking of a Pt layer and Bi bilayer along the $c$ axis. The compound crystallizes in space group $P\bar{3}$ with a hexagonal unit cell of $a = b = 6.553$ Å, $c = 6.165$ Å. Its $T$-dependent resistivity is typical of a metal whereas a large anisotropy was observed for the in-plane and interplane electrical transport. The magnetization data show opposite sign for fields parallel and perpendicular to the Pt layers, respectively. The magnetic field response of this material shows clearly two types of charge carriers, consistent with the multiple Fermi surfaces revealed in our band structure calculations. The hydrostatic pressure is shown to suppress the resistivity at high $T$ systematically but has little bearing on its low-$T$ transport. Through calorimetric measurements, the density of states at the Fermi level and the Debye temperature are determined to be 0.94 $eV^{-1}$ per molecule and 145 K, respectively. In addition, the electronic structures and parity analyses are also presented. We find a minimum value of 0.05 eV gap opening at around 2 eV under the Fermi level by invoking spin-orbit interaction. A slab calculation further indicates a surface Dirac cone appearing in the gap of bulk states. We discuss the possibility of $PtBi_2$ being a candidate for a bulk topological metal, in analogy to the recently proposed topological superconductor $\beta$-$PdBi_2$.

DOI: 10.1103/PhysRevB.94.165119

## I. INTRODUCTION

Binary bismuthide $\beta$-$PdBi_2$ has attracted much interest recently as a promising candidate for topological superconductor (TS) [1–7]. Topological superconductivity is a new state of matter possessing symmetry-protected surface states while the bulk states are fully gapped by superconducting pairing [8–11]. The Majorana fermions are believed to exist on the surface or vortex core in such TSs, which may not only be of scientific importance, but also can lead to wide-ranging applications in microelectronic devices and quantum computing. The centrosymmetric stoichiometric $\beta$-$PdBi_2$ ($T_c \sim 5$ K) was recently claimed to be topologically nontrivial in view of the observation of the topologically protected surface modes by spin- and angle-resolved ARPES [4]. However, no Andreev bound states associated with Majorana fermions are detectable through point-contact spectroscopy [7], in sharp contrast to the cases in Cu-intercalated $Bi_2Se_3$ [12,13] and In-doped SnTe [14]. On the other hand, it becomes the common wisdom that spin-orbit interaction (SOI) in heavy elements is crucial for the topological states. It is therefore heuristic to ask what if we replace Pd in $PdBi_2$ with a heavier Pt element to enhance SOI.

In this study, we substituted Pt for Pd in $PdBi_2$ and found that this new material actually crystallizes in a distinct structure. Unlike $\beta$-$PdBi_2$, which has the tetragonal structure in an $I4/mmm$ space group, $PtBi_2$ crystallizes in space group $P\bar{3}$ with a hexagonal unit cell of $a = b = 6.553$ Å, $c = 6.165$ Å [15], as shown in Fig. 1. It is also different from its homologue PtBi superconductor ($T_c = 1$ K) with a monoclinic unit cell [16]. The $T$-dependent resistivity of $PtBi_2$ shows metallic behaviors down to 2 K, and displays a large anisotropy for the in-plane and interplane transport. The intraplane and interplane magnetization exhibits extreme anisotropy, being diamagnetic with the field aligned along the basal plane and paramagnetic when the field is normal to the plane. The magnetoresistance (MR) and Hall resistivity measured on the same sample both show two types of carriers and the former one scales well to the one form of semiclassical Kohler's rule [17,18], i.e., $\frac{\Delta\rho}{\rho} = F(\frac{B}{\rho})$. The heat capacity and the pressure effects on resistivity have also been investigated. Additionally, our first-principles calculations reveal multiple bands crossing the Fermi level and the prominent effects of SOI on its band structure. Importantly, a sizable gap is opening at around 2 eV under the Fermi level by including the SOI, similar to what was seen in $\beta$-$PdBi_2$. The parity analyses indicate this gap opening has a nontrivial consequence for the surface states, which was further confirmed by our slab calculations.

## II. EXPERIMENT

$PtBi_2$ single crystals were fabricated via a melt-growth method. The starting materials of high-purity Bi powder ($4N$) and Pt powder ($4N$) were mixed thoroughly in the prescribed molar ratio of Bi:Pt = 2:1 (2 g in total weight). All these preparations were performed in a glove box filled with protective argon gas (both $H_2O$ and $O_2$ contents were limited below 0.1 ppm). The mixtures were loaded and sealed in an evacuated quartz tube. This quartz tube was then heated to 700 °C quickly in a sintering furnace and kept at this temperature for 48 h, before being slowly cooled down to 450 °C(3 °C/h), and finally being quenched into cold water.

*Corresponding author: xiaofeng.xu@hznu.edu.cn

†Corresponding author: libin@njupt.edu.cn

 

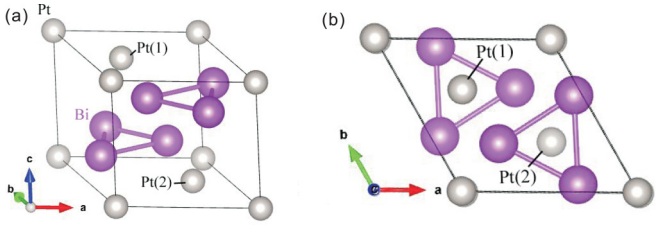


FIG. 1. Crystal lattice of $PtBi_2$. (a) The primitive unit cell for hexagonal $PtBi_2$. The coordinates of Pt(1) and Pt(2) are $(\frac{a}{3}, \frac{2a}{3}, 0.92c)$ and $(\frac{2a}{3}, \frac{a}{3}, 0.08c)$, respectively. (b) The structure as seen from a perspective along the $c$ axis.

Large pieces of dark gray platelike $PtBi_2$ single crystals of typical 7–8 mm in length were harvested.

Energy dispersive x-ray (EDX) spectrometry confirms the stoichiometric ratio of the chemical composition ($32.8 : 67.2 \pm 1.0\%$ in molar percentage for Pt:Bi). A typical EDX spectrum is given in the Supplemental Material (SM) [19]. The structure of crystals was characterized by x-ray diffraction (XRD) at room temperature using a Rigaku diffractometer with Cu $K\alpha$ radiation and a graphite monochromator. Lattice parameters were obtained by Rietveld refinements. The magnetization was measured by vibrating sample magnetometry using a Quantum Design MPMS-5 system. Measurements of MR and Hall effect were performed on the same sample by changing the field polarities. The even signal in field was defined as MR and the odd component was calculated as Hall resistivity. For the hydrostatic pressure measurements, a commercial piston-type cell from Quantum Design was used, and Daphne 7373 oil was applied as the pressure transmission media. The same electrical contacts were used throughout the measurements such that the geometric errors in the contact size were identical for all pressures. The specific heat measurement was performed on a large piece of single crystal of weight 3.5 mg. The thermometer on the calorimeter puck was well calibrated prior to the measurements and the addenda was determined in a separate run.

Based on our experimental crystal structure, we carry out first-principles calculations for the band structures and topological invariant. The electronic structure calculations with high accuracy are performed using the full-potential linearized augmented plane wave (FP-LAPW) method implemented in the WIEN2K code [20]. The generalized gradient approximation (GGA) [21] is applied to the exchange-correlation potential calculation. The muffin-tin radii are chosen to be 2.5 a.u. for both Pt and Bi. The plane-wave cutoff is defined by $RK_{max} = 7.0$, where R is the minimum LAPW sphere radius and $K_{max}$ is the plane-wave vector cutoff.

## III. RESULTS

### A. Crystal structure

The schematic view of the crystal structure of $PtBi_2$ is shown in Fig. 1. It crystallizes in a hexagonal structure with the space group $P3$ (No. 147). Its structure consists of alternate stacking of two-dimensional (2D) Pt layers and bismuth bilayers along the $c$ axis. In one primitive unit cell, there are three Pt atoms, one being located at the corner of the polyhedron and the other two being labeled as Pt(1) and Pt(2) in Fig. 1. The Bi atoms are trigonally coordinated. The XRD patterns of $PtBi_2$ crystal are presented in Fig. 2. A small trace of impurity phase, marked by the asterisks in Fig. 2(a), is detectable in the powder x-ray pattern but is absent in the single-crystal XRD. Only $(00\ell)$ diffraction peaks are observed in the single-crystal x ray, indicating good $c$-axis orientation of the as-grown samples. The calculated lattice parameters are $a = b = 6.553$ Å, $c = 6.165$ Å, in consistence with previous reported results [15]. Note here that the other polymorphs of $PtBi_2$, namely $\alpha$-$PtBi_2$ (orthorhombic), $\beta$-$PtBi_2$ (cubic), and $\delta$-$PtBi_2$ (orthorhombic), can be precluded as the main phases of our sample, based on our powder x-ray pattern [22].

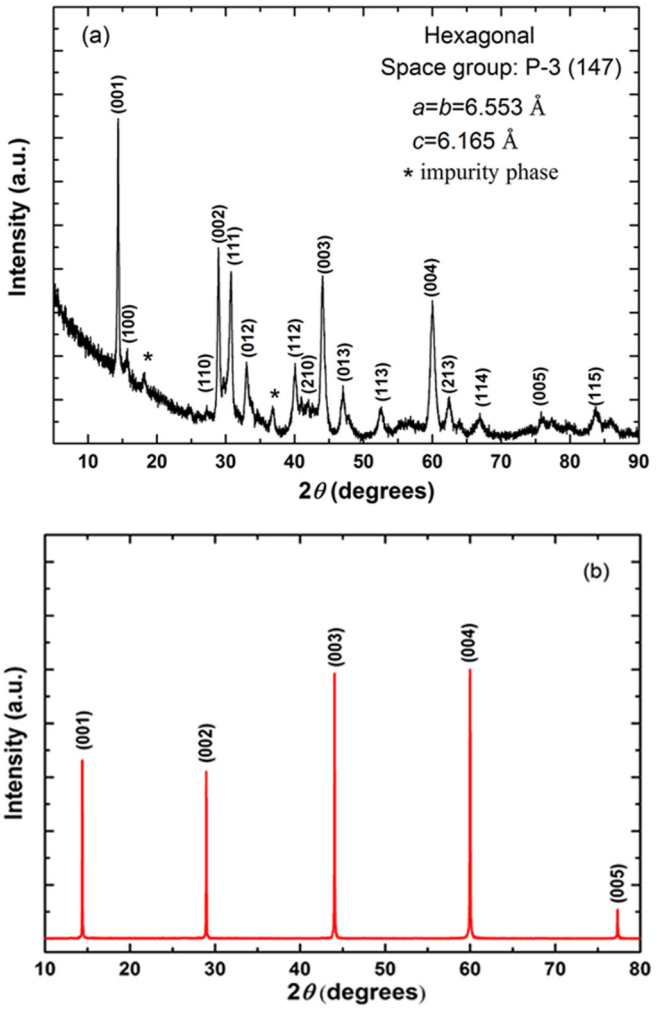


FIG. 2. (a) and (b) represent the powder XRD patterns and single-crystal XRD diffraction peaks, respectively. The asterisks in (a) mark the impurity phase that is possibly $\alpha$-$PtBi_2$.

### B. Anisotropic transport and susceptibility

Zero-field resistivity is plotted in Fig. 3. Both the in-plane [Fig. 3(a)] and interplane [Fig. 3(b)] resistivity are metallic down to the lowest temperature measured (2 K). The residual resistivity ratio (RRR) is approximately 50 (22) for in-plane (interplane) transport. As a comparison, RRR in $\beta$-$PdBi_2$ ranges from 3–10 in the literature. The resistivity anisotropic ratio ($\rho_c/\rho_{ab}$) increases from ~70 at room temperature to

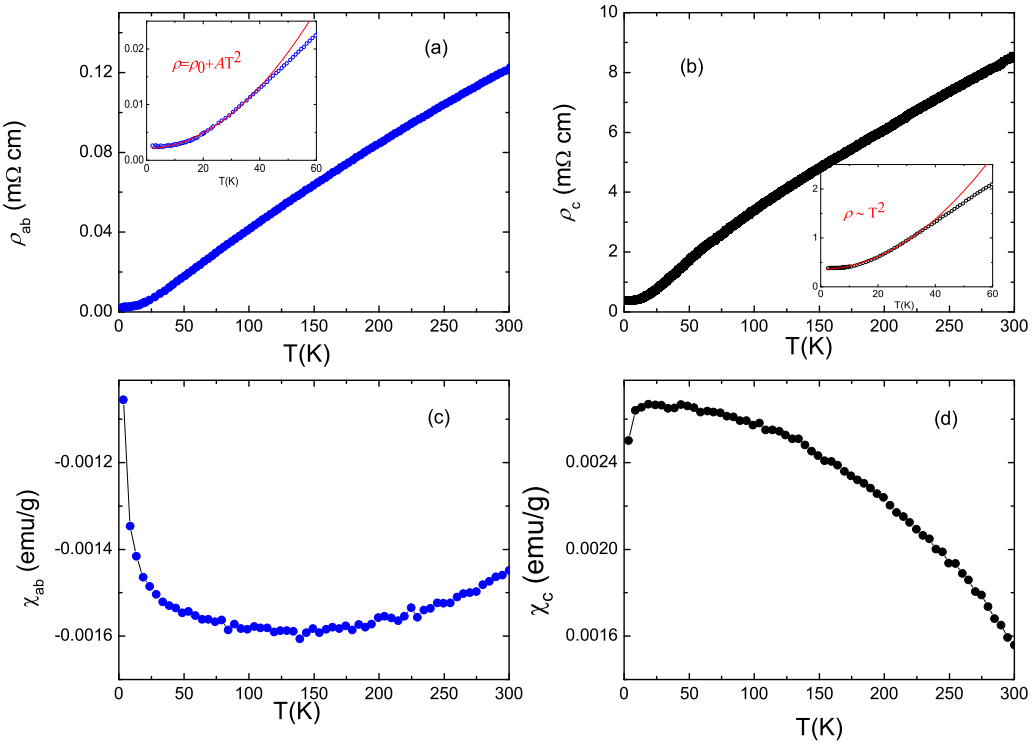


FIG. 3. (a) In-plane and (b) interplane zero-field resistivity curves down to 2 K. The low-$T$ resistivity fits to $\rho = \rho_0 + AT^2$ very well below ~35 K (see the insets to each panel). (c) and (d) show the in-plane and inter-plane susceptibility under a field of 0.5 Tesla, respectively.

~150 at 2 K. Despite this large resistivity anisotropy, the interplane transport remains coherent at low temperatures, evidenced by a Fermi-liquid $T^2$ scaling below ~30 K in both cases. We estimated the electron mean-free path $l_0$ of this sample from its in-plane residual resistivity ($\rho_0 = 2.5\mu\Omega$cm) and the Drude formula $\sigma = \frac{ne^2\tau}{m}$, where $n = 4.26 \times 10^{26}/\text{m}^3$ from the band structure calculations (see below). $l_0$ has an order of ~1$\mu$m at 2 K, two orders of magnitude larger than that in $\beta$-$PdBi_2$ [3]. The sample was further characterized by the susceptibility measurements thereafter. Remarkably, the magnetization of the sample shows extreme anisotropy with respect to the field orientations. As illustrated in Fig. 3, the in-plane magnetization $\chi_{ab}$ is diamagnetic and varies little with $T$ down to 20 K, below which it displays a significant upturn, whereas the interplane $\chi_c$ is paramagnetic instead and increases monotonically with decreasing $T$, followed by a downward trend below 20 K. The origin of these contrasting magnetization behaviors is not clear at this stage. Given the rather small susceptibility in our sample and the diverse contributions at this $T$ range, e.g., Pauli and Landau susceptibilities, it may be not so unusual to have the opposite signs for the different field orientations.

### C. Magnetoresistance and Hall effect

The magnetoresistive and Hall response of a material can open an avenue for exploring the dispersion and dynamics of the charge carriers. We performed the MR and Hall measurements with the same electrical contacts on a sample with $RRR = 65$ as shown in Fig. 4. First, in $PtBi_2$, it is noted that the absolute value of the MR, defined as $\frac{\Delta\rho}{\rho}$, is rather large, reaching $> 400\%$ at 2 K in a magnetic field of 9 T. This large MR implies a rather large electron mean-free path, hence a long relaxation time. However, this MR is damped very fast with increasing $T$, as seen from the top panels of Fig. 4. Second, in single-band metals, the MR at small fields is usually quadratic and the Hall resistivity varies linearly with field. However, in the two-band Drude model, on the assumption of the field-independent carrier density and relaxation time, $\frac{\Delta\rho}{\rho}(B)$ and $\rho_{xy}(B)$ can be written as [23–26]

$$\frac{\Delta\rho}{\rho} = \frac{\sigma_h\sigma_e(\sigma_h R_h - \sigma_e R_e)^2 B^2}{(\sigma_h+\sigma_e)^2 + \sigma_h^2\sigma_e^2(R_h+R_e)^2 B^2} \quad (1)$$

$$\rho_{xy}(B) = \frac{\sigma_h^2 R_h + \sigma_e^2 R_e + \sigma_h^2\sigma_e^2 R_h R_e (R_h+R_e) B^2}{(\sigma_h+\sigma_e)^2 + \sigma_h^2\sigma_e^2(R_h+R_e)^2 B^2} B, \quad (2)$$

where $\sigma_e(h)$ and $R_e(h)$ are electrical conductivity and Hall coefficient for electron (hole) band, respectively. The MR and the Hall signal for $PtBi_2$ samples are exemplified in Fig. 4 at some selected temperatures. Although the individual curves can be fitted with the above two-band equations reasonably well, plotted as the red solid line in each panel, we failed to model these two transport coefficients simultaneously with the same set of four parameters. These difficulties may arise from the simple assumption of the field-independent charge carrier density and scattering, or from the complex FS more than just two bands. In cuprate $Pr_{2-x}Ce_xCuO_{4-\delta}$, similarly, it was unlikely to fit the MR and Hall resistivity simultaneously with the same set of fitting parameters, but can only be fitted separately [23]. Nevertheless, given the quality of our fitting and the strong nonlinearity of the Hall resistivity, we believe that the transport properties of this compound are governed by multiband charge carriers, consistent with the multiple electron

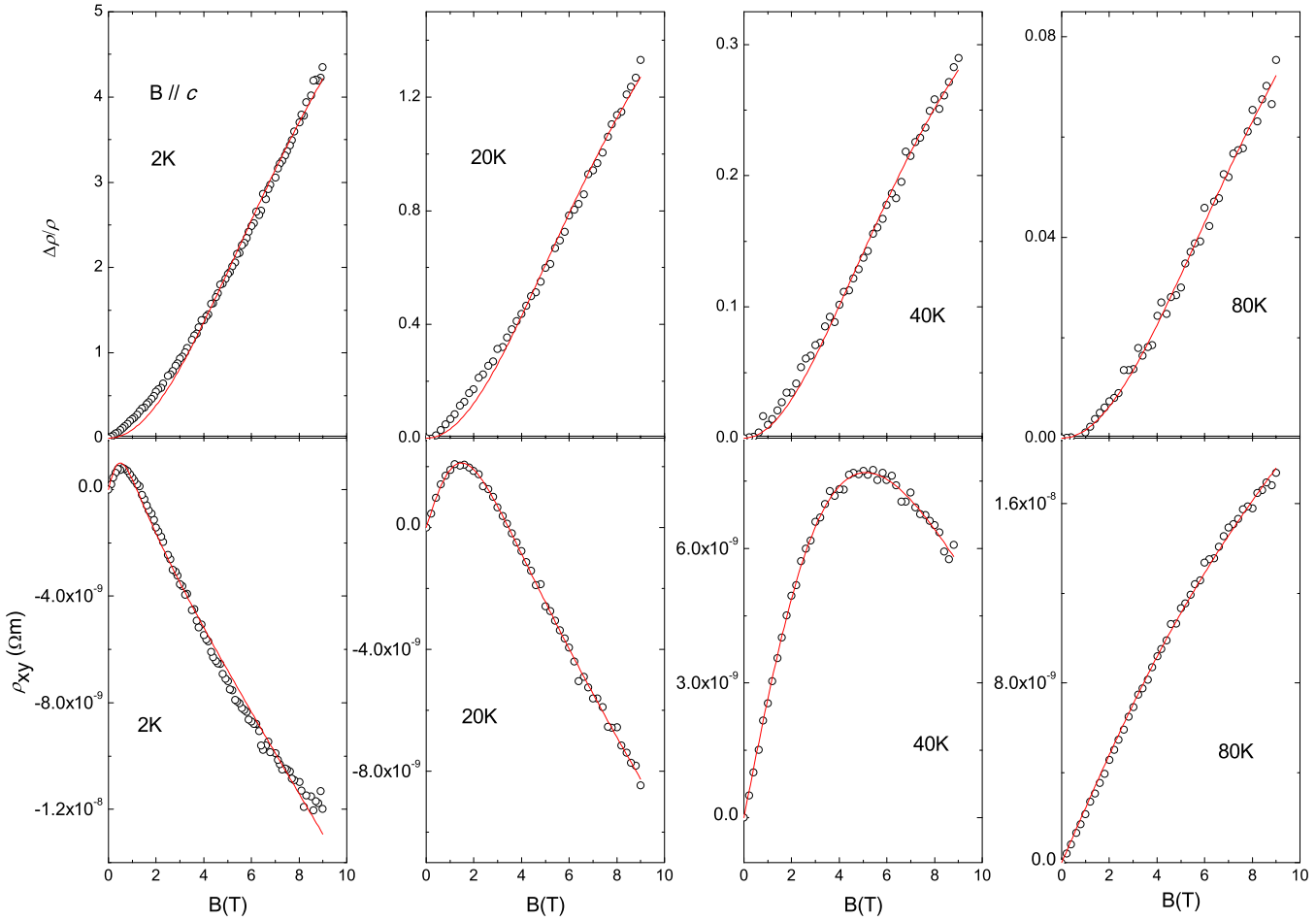


FIG. 4. The magnetoresistance (top panel) and Hall resistivity (bottom panel), both measured on the same crystal with the same electrical contacts, at several selected temperatures. The red solid curves delineate the fits to the two-band carrier model.

and hole Fermi pockets revealed by our band calculations (see below). Indeed, as shown in the SM, the three-band model significantly improves the overall fitting quality below 40 K. We also note that our transport data have marked difference from those reported in Ref. [27], where the linear MR arises from the sample inhomogeneity due to sufficient Bi vacancies [28], in contrast with the chemical stoichiometry in our samples.

In standard metals, the MR $\Delta\rho/\rho$ at a certain temperature under a field $H$ has a general form known as the Kohler's rule [17,18]: $\Delta\rho/\rho = f(B\tau)$. This rule adopts a simplified form $\Delta\rho/\rho = F(B/\rho)$ on the assumption of $T$-independent carrier density $n$ and a constant effective mass $m^*$. From this rule, $\Delta\rho/\rho$ is literally independent of $T$ such that the plots of $\Delta\rho/\rho_0$ as a function of $B/\rho$ at distinct temperatures will collapse onto a single curve. Interestingly, this rule, despite its semiclassical origin, was found to be well obeyed in a large number of metals from conventional metals to some quantum matters. These involve the metals with two types of carriers [18], the pseudogap phase of the underdoped cuprates [29], quasi-one-dimensional metals [30,31] as well as some topological semimetals [32]. We examined this simplified Kohler's rule in $PtBi_2$ (Fig. 5) and found that it is well obeyed in this material, over a wide field range (up to 9 T) and a broad $T$ window (2–100 K. Above 100 K, the MR tends to be negligible). Moreover, the longitudinal MR in $PtBi_2$ (B ∥ I ∥ $ab$) also shows two types of charge carriers and the validity of the simplified Kohler's rule (see SM). As pointed out in Ref. [18], however, care needs to be taken in using this simplified form of Kohler's rule as $n$ and $m^*$ may be

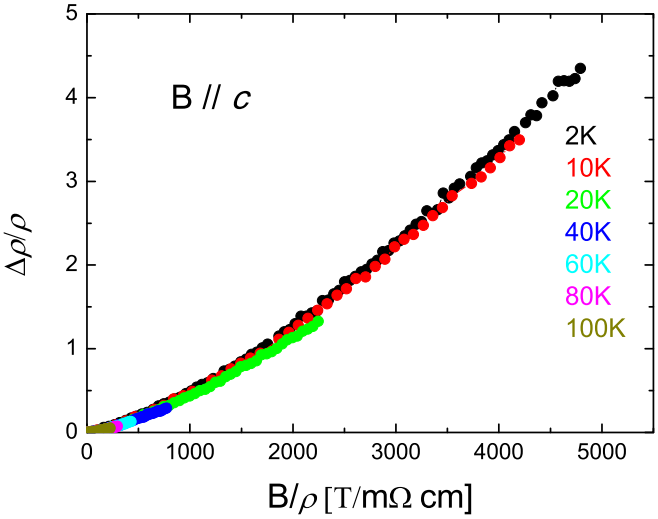


FIG. 5. The Kohler's plot for the MR data from Fig. 4.

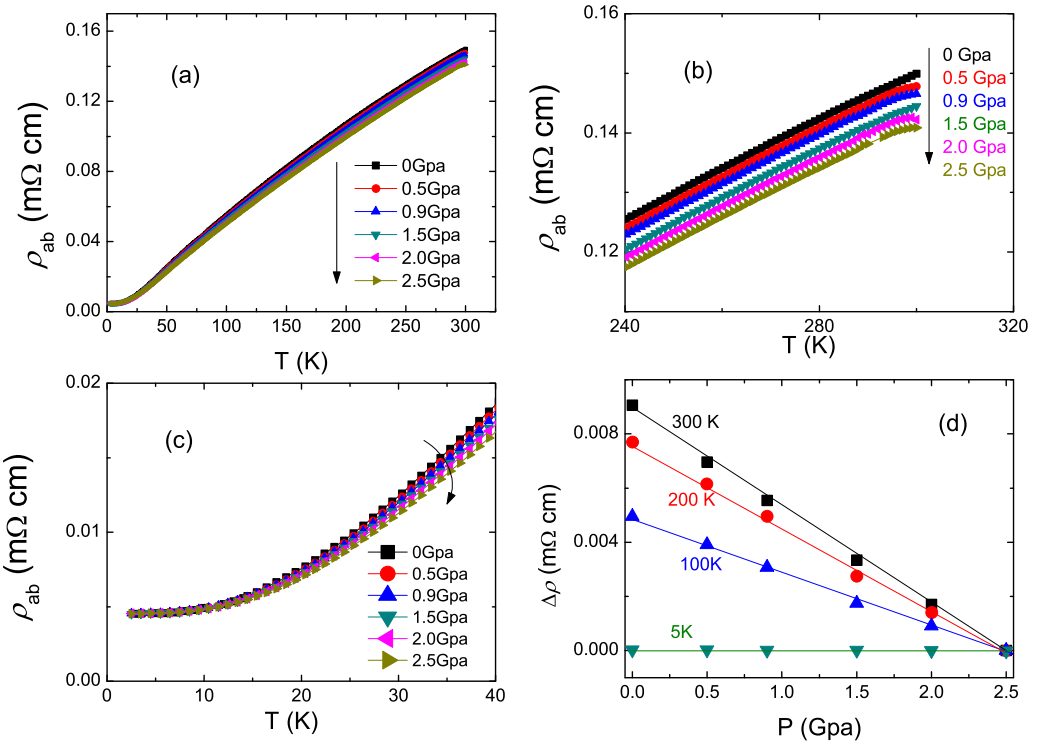


FIG. 6. (a) The resistivity $\rho(T)$ profiles under different pressures. (b) and (c) zoom in the high-$T$ and low-$T$ regimes, respectively. (d) The pressure dependence of resistivity at some temperatures. $\Delta\rho$ is measured with respect to the value at 2.5 Gpa.

$T$ dependent. With these caveats in mind, it could not be concluded if the Kohler's rule is really obeyed or violated in $PtBi_2$, unless the full knowledge of its $n(T)$ and $m^*(T)$ becomes available.

### D. Pressure dependence of resistivity

Figure 6 depicts the zero-field resistivity $\rho(T)$ curves under various pressures for a crystal that has slightly larger resistivity value ($\rho_0 = 4.5$ $\mu\Omega$cm at 2 K) and a lower RRR (33). As seen, the pressure suppresses the resistivity at high $T$ progressively [Fig. 6(b)] and this pressure effect fades with decreasing temperatures [Fig. 6(c)], becoming negligibly small below ~15 K. It is noted that pressure suppresses the resistivity in a linear fashion, plotted in Fig. 6(d) with $\Delta\rho$ defined as the resistivity difference from the value under 2.5 Gpa at each temperature. It is noteworthy that this pressure effect resembles what was observed in $\beta$-$PdBi_2$ where the normal state resistivity diminishes systematically as pressure increases [2].

### E. Specific heat

As shown in Fig. 7(a), the heat capacity $C(T)$ down to 0.5 K decreases smoothly with $T$ and shows no clear features at this temperature regime. The heat capacity at low $T$ comprises the electronic contribution $\gamma T$ and the phononic term $\beta T^3$. The fitting below ~3 K [Fig. 7(b)] yields $\gamma = 2.2$ mJ/mol $K^2$ and $\beta = 1.94$ mJ/mol $K^4$, corresponding to the density of state (DOS) at the Fermi level 0.94 $eV^{-1}$ per molecule and the Debye temperature $\Theta_D = 145$ K. As a comparison, $\gamma$ in $\beta$-$PdBi_2$ is a factor of 6 higher than here and the Debye

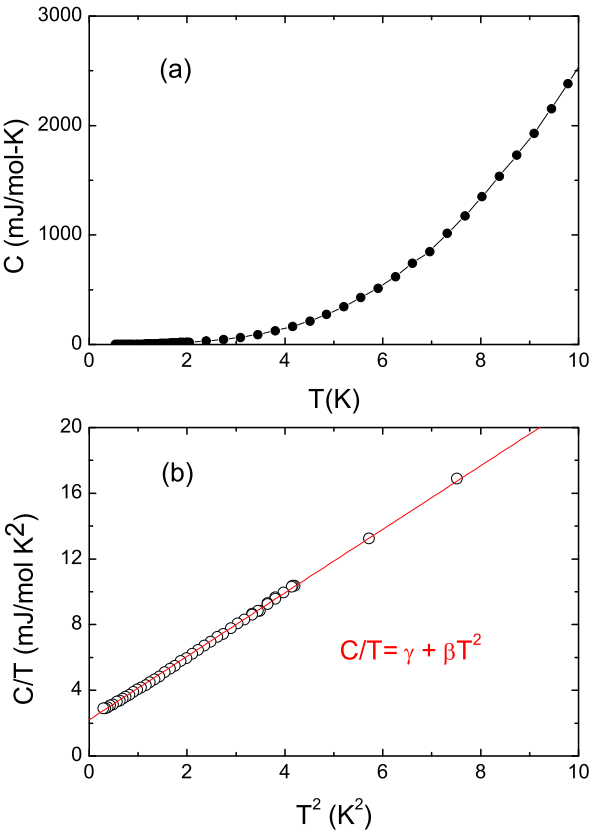


FIG. 7. (a) Heat capacity of $PtBi_2$ between 0.5 K and 10 K. (b) The plot of $C/T$ vs $T^2$ at low temperatures to separate the electronic and phonon contributions. The red line is the fit to $C/T = \gamma + \beta T^2$.

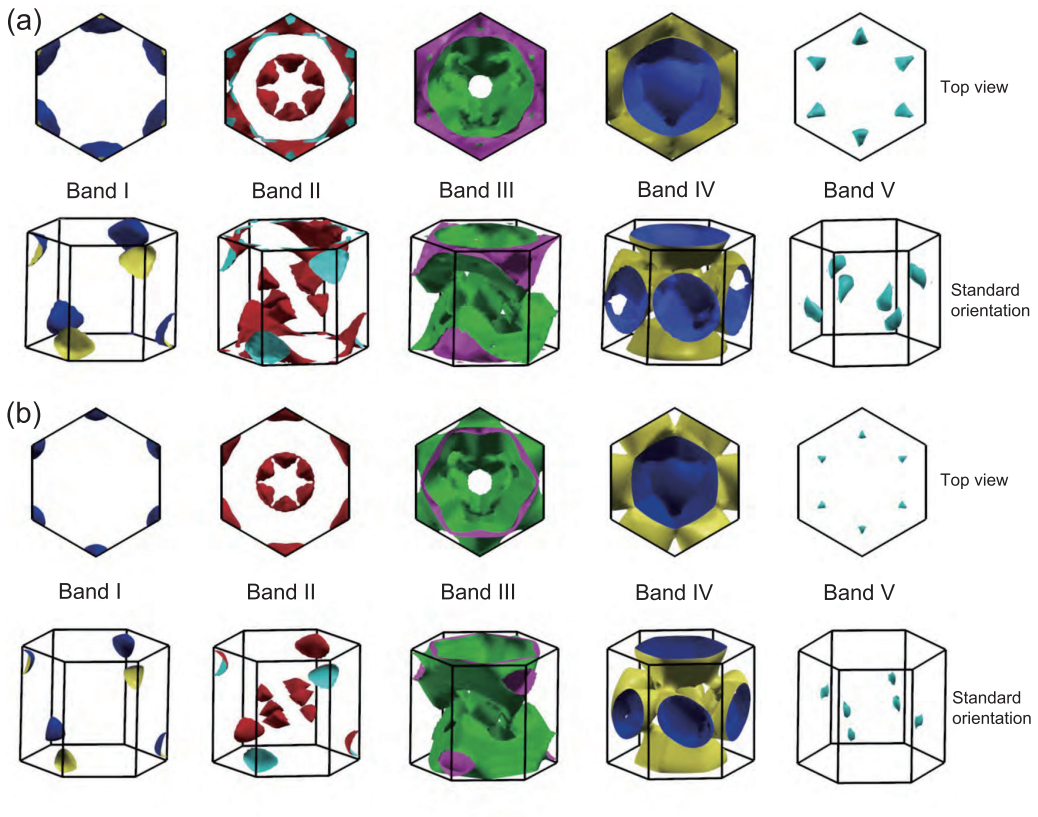


FIG. 8. Three-dimensional Fermi surfaces of $PtBi_2$ in the first Brillouin zone: (a) scalar-relativistic case (without SOI), (b) relativistic case (with SOI). Each panel shows five FS sheets in scalar-relativistic and relativistic cases, respectively.

temperature is comparable (136 K) [1,5]. The reproducibility of the data presented here has been confirmed on different crystals.

### F. Band structures

Our band structure calculations show that there are five bands crossing $E_F$. Figure 8 shows the corresponding FSs drawn using XCRYSDEN [33]. In order to get the electronic FS of high resolution, we used a $35 \times 35 \times 32$ $k$ mesh with about 40000 $k$ points to calculate the eigenenergies, which are accurate enough to evaluate the results. For each case, we present the five FSs with top view (projected along the $\Gamma$–$A$ direction) and standard orientation view. The FSs show clearly hexagonal symmetry in the first Brillouin zone. When SOI was taken into account, all FSs shrink noticeably due to the change of the band structure. The FS analysis has been performed to determine the band type using SKEAF (Supercell K-space Extremal Area Finder) [34]. Without SOI, band I and II are 100% holelike. Band III is mixed with 62.2% electronlike and 37.8% holelike types. Band IV is 90.4% electronlike and 9.6% holelike, and band V is 100% electronlike. In relativistic case (with SOI), the types of band I, II, and V are the same as in the scalar relativistic case. Band III is 61.5% electronlike and 38.5% holelike, while band IV is 93.4% electronlike and 6.6% holelike.

From the calculations, the values of DOS at $E_F$ are $N(E_F) = 1.53$ and 1.71 states/eV per formula unit for the scalar relativistic (without SOI) and relativistic (with SOI) calculations, respectively. The corresponding electronic specific heat coefficient $\gamma$ [$\gamma = \pi^2 N(E_F) k_B^2/3$] are 3.6 and 4.0 mJ/mol $K^2$, respectively. Note this $\gamma$ is almost twice the value obtained from heat capacity measurements. Usually, the experimental $\gamma$ is $(1 + \lambda)$ times of the value obtained from the calculations due to the renormalization effects from the electron-phonon and/or electron-electron interactions, where $\lambda$ is the coupling constant. The smaller value of $\gamma$ from the experiment in $PtBi_2$ is somewhat strange and deserves further investigations.

Our results on the bulk band structures with and without SOI are shown in Figs. 9(a) and 9(b), respectively. The bands are numbered from first to eighth by the energy at the $A$ point on the right side of the graphs. Note that, without SOI, band 4 and 5, band 6 and 7 are degenerate. That means they have the same energy and symmetry (see Table I). According to the orbital-colored characteristics of the fat bands, hybridized Bi $6p$ and Pt $5d$ bands distribute around the Fermi level. While below $-2.0$ eV, Pt $5d$ orbitals dominate the band structure. By comparing Figs. 9(a), 9(b), we found a continuous gap [shaded by pink in Fig. 9(b)] throughout the Brillouin zone, with a minimum value of 0.05 eV gap opening. The first and second bands that lie below and above the gap are completely separated from each other. The gap opening by SOI is crucial for the possible topological property of $PtBi_2$.

To evaluate the possible topologically nontrivial surface states, we use the method proposed by M. Sakano *et al.* [4] to compute the $Z_2$ invariants. With $P3$ symmetry of $PtBi_2$,

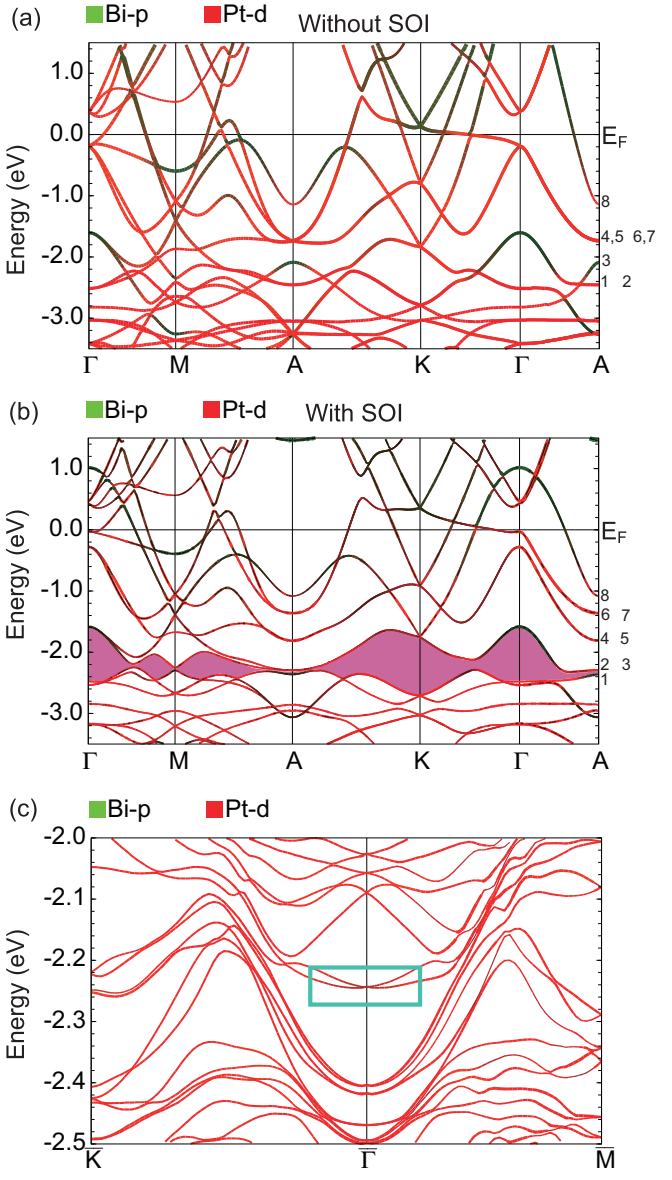


FIG. 9. First-principles band structures (a) without and (b) with spin-orbit interaction. The green and red lines indicates the Bi-$p$ and Pt-$d$ orbital contributions, respectively. The band numbers are listed on the right side. The pink-shaded area in (b) denotes the gap induced by SOI. (c) Surface band dispersions along $\bar{K}$–$\bar{\Gamma}$–$\bar{M}$ obtained by slab calculation of three $(PtBi_2)_3$ layers. The blue rectangle indicates the region where the surface state appears.

$Z_2$ can be calculated by considering solely $\Gamma(0, 0, 0)$and $A(0, 0, \pi)$ points. The point group for these two points is $C_{3i}$, which has six symmetry operations in six classes. We list the topological invariant $Z_2$ and the symmetries of wave functions for respective bands in Table I. The calculated $Z_2 = 1$ indicates the topologically nontrivial band state of $PtBi_2$. This requires a surface state connecting the bands of the gap. The topological surface state is further evidenced by the calculated slab band structure in Fig. 9(c). As one $PtBi_2$ crystalline unit cell (Fig. 1) has three formula units as $(PtBi_2)_3$, we cleave a three-$(PtBi_2)_3$-layer slab in (001) plane with 15 Å vacuum layer for the calculation. The blue rectangle

TABLE I. Lists of the topological invariant and the symmetries of wave functions at Γ and A points without and with SOI.

| | Without SOI | | | With SOI | | |
|---|---|---|---|---|---|---|
| # | Γ | $A$ | $Z_2$ | Γ | $A$ | $Z_2$ |
| 1 | $A_u$ | $A_u$ | 0 | ${}^1E_{1/2g} + {}^2E_{1/2g}$ | ${}^1E_{1/2u} + {}^2E_{1/2u}$ | 1 |
| 2 | $A_u$ | $A_g$ | 1 | ${}^1E_{1/2u} + {}^2E_{1/2u}$ | ${}^1E_{1/2g} + {}^2E_{1/2g}$ | 0 |
| 3 | $A_g$ | $A_u$ | 0 | ${}^1E_{1/2g} + {}^2E_{1/2g}$ | ${}^1E_{1/2u} + {}^2E_{1/2u}$ | 1 |
| 4 | ${}^2E_u + {}^1E_u$ | ${}^2E_g + {}^1E_g$ | 1 | $A_{3/2u} + A_{3/2u}$ | $A_{3/2g} + A_{3/2g}$ | 0 |
| 5 | ${}^2E_u + {}^1E_u$ | ${}^2E_g + {}^1E_g$ | 0 | $A_{3/2g} + A_{3/2g}$ | $A_{3/2u} + A_{3/2u}$ | 1 |
| 6 | ${}^2E_g + {}^1E_g$ | ${}^2E_u + {}^1E_u$ | 1 | ${}^1E_{1/2u} + {}^2E_{1/2u}$ | ${}^1E_{1/2g} + {}^2E_{1/2g}$ | 0 |
| 7 | ${}^2E_g + {}^1E_g$ | ${}^2E_u + {}^1E_u$ | 0 | ${}^1E_{1/2g} + {}^2E_{1/2g}$ | ${}^1E_{1/2u} + {}^2E_{1/2u}$ | 1 |
| 8 | ${}^2E_u + {}^1E_u$ | $A_g$ | 1 | $A_{3/2u} + A_{3/2u}$ | ${}^1E_{1/2g} + {}^2E_{1/2g}$ | 0 |

in Fig. 9(c) encircles the region where the surface state appears in the bulk gap at the energy of −2.24 eV at $\bar{\Gamma}$, below the minimum energy detected in recent ARPES measurements [28]. From Table I, we found that bulk gap between first and second bands is characterized by $Z_2(\#1) = 1$, indicating its analogy to 3D strong topological insulators. Thus, the connection represents a topologically protected surface state.

## IV. DISCUSSION AND CONCLUSIONS

In recent work by Sakano *et al.*, several topologically-protected surface states were observed by spin-resolved ARPES in the TS candidate $\beta$-$PdBi_2$ [4]. These nontrivial surface bands include one crossing the Fermi level and the other one forming the Dirac cone state 2 eV below the Fermi level. It was noted that these topological surface states are all derived as a consequence of SOI, although their respective microscopic details may be different. In $PtBi_2$, the SOI plays a similar role and manifests itself in the band structure as a gap opening ∼2 eV below the Fermi level, in which the topologically nontrivial surface states may arise. Interestingly, this material was reported to superconduct below 150 mK [35], a factor of ∼40 lower than $T_c$ in $PdBi_2$. How the possible nontrivial surface states of $PtBi_2$ condense into Cooper pairs in the superconducting state await more investigations, both theoretically and experimentally.

In $PtBi_2$, the electrical transport presented here is overall dominated by its bulk normal electrons and it looks more like a conventional multiband metal from transport perspective. Likewise, the transport and thermodynamic signatures from the surface states in $\beta$-$PdBi_2$ are also very weak, or lack thereof. Its superconductivity is characterized by a nodeless, single $s$-wave energy gap of strong coupling nature. This dilemma is partly due to the fact that in both cases, the surface Dirac cone lies far below the Fermi level therefore the bulk transport dominates. In order to observe the surface property from the bulk transport, it may be necessary to push the Fermi level into the SOI gap by using electrical gating in a heterostructure geometry.

To summarize, we synthesized the single crystals of stoichiometric bismuthide $PtBi_2$ by a solid-state reaction method. The samples were carefully characterized by the combined

procedures of XRD, (magneto)transport, susceptibility, heat capacity, and hydrostatic pressure measurements. MR and Hall resistivity of this compound show prominent multiband transport behaviors, consistent with the multiple Fermi electron and hole pockets revealed in our first-principles calculations. The possible topological surface state of $PtBi_2$ is revealed by the $Z_2$ analysis and confirmed in the slab band calculations. Both band structures and $Z_2$ invariant calculations suggest $PtBi_2$ as a possible candidate for a bulk topological metal. Further experiments, especially ones with more surface sensitivity, are needed to search for the possible surface states in this bismuthide.

## ACKNOWLEDGMENTS

The authors would like to thank C. M. J. Andrew and A. F. Bangura for stimulating discussions. This work is sponsored by the National Key Basic Research Program of China (Grant No. 2014CB648400), and by National Natural Science Foundation of China (Grants No. 11474080, No. U1432135, No. 11611140101, No. 11504182, and No. 11374257). X.X. would also like to acknowledge the financial support from the Distinguished Young Scientist Funds of Zhejiang Province (LR14A040001), Natural Science Foundation of Jiangsu Province (BK20150831), and an open program from Wuhan National High Magnetic Field Center (2015KF15).

[1] Y. Imai, F. Nabeshima, T. Yoshinaka, K. Miyatani, R. Kondo, S. Komiya, I. Tsukada, and A. Maeda, J. Phys. Soc. Jpn. **81**, 113708 (2012).
[2] K. Zhao, B. Lv, Y. Y. Xue, X. Y. Zhu, L. Z. Deng, Z. Wu, and C. W. Chu, Phys. Rev. B **92**, 174404 (2015).
[3] E. Herrera *et al.*, Phys. Rev. B **92**, 054507 (2015).
[4] M. Sakano, K. Okawa, M. Kanou, H. Sanjo, T. Okuda, T. Sasagawa, and K. Ishizaka, Nature Commun. **6**, 8595 (2015).
[5] J. Kačmarčík *et al.*, Phys. Rev. B **93**, 144502 (2016).
[6] P. K. Biswas *et al.*, Phys. Rev. B **93**, 220504 (2016).
[7] L. Q. Che, T. Le, C. Q. Xu, X. Z. Xing, Z. X. Shi, Xiaofeng Xu, and Xin Lu, Phys. Rev. B **94**, 024519 (2016).
[8] M. Z. Hasan and C. L. Kane, Rev. Mod. Phys. **82**, 3045 (2010).
[9] Y. S. Hor, A. J. Williams, J. G. Checkelsky, P. Roushan, J. Seo, Q. Xu, H. W. Zandbergen, A. Yazdani, N. P. Ong, and R. J. Cava, Phys. Rev. Lett. **104**, 057001 (2010).
[10] Liang Fu, C. L. Kane, Phys. Rev. B **76**, 045302 (2007).
[11] Liang Fu, C. L. Kane, E. J. Mele, Phys. Rev. Lett. **98**, 106803 (2007).
[12] M. Kriener, K. Segawa, Z. Ren, S. Sasaki, and Y. Ando, Phys. Rev. Lett. **106**, 127004 (2011).
[13] S. Sasaki, M. Kriener, K. Segawa, K. Yada, Y. Tanaka, M. Sato, and Y. Ando, Phys. Rev. Lett. **107**, 217001 (2011).
[14] M. Novak, S. Sasaki, M. Kriener, K. Segawa, and Y. Ando, Phys. Rev. B **88**, 140502 (2013).
[15] T. Biswas and K. Schubert, J. Less Common Metals **19**, 223 (1969).
[16] B. T. Matthias, Phys. Rev. **92**, 874 (1953).
[17] M. Kohler, Ann. Phys. **424**, 211 (1938).
[18] N. Luo, and G. H. Miley, Physica C **371**, 259 (2002).
[19] See Supplemental Material at http://link.aps.org/supplemental/10.1103/PhysRevB.94.165119 for a typical EDX spectrum.
[20] P. Blaha, K. Schwarz, G. K. H. Madsen, D. Kvasnicka, J. Luitz, WIEN2K, An Augmented Plane Wave LO Program for Calculating Crystal Properties, TU Wien, Vienna, 2001.
[21] J. P. Perdew, K. Burke, and M. Ernzerhof, Phys. Rev. Lett. **77**, 3865 (1996).
[22] X. Z. Li, P. Kharel, V. R. Shaha, and D. J. Sellmyer, Philos. Mag. **91**, 3406 (2011).
[23] P. Li, F. F. Balakirev, and R. L. Greene, Phys. Rev. Lett. **99**, 047003 (2007).
[24] F. Rullier-Albenque, D. Colson, A. Forget, and H. Alloul, Phys. Rev. Lett. **103**, 057001 (2009).
[25] P. M. C. Rourke, A. F. Bangura, C. Proust, J. Levallois, N. Doiron-Leyraud, D. LeBoeuf, L. Taillefer, S. Adachi, and M. L. Sutherland, and N. E. Hussey, Phys. Rev. B **82**, 020514(R) (2010).
[26] F. Rullier-Albenque, D. Colson, A. Forget, and H. Alloul, Phys. Rev. Lett. **109**, 187005 (2012).
[27] X. J. Yang *et al.*, Appl. Phys. Lett. **108**, 252401 (2016).
[28] Q. Yao *et al.*, arXiv:1607.03381.
[29] M. K. Chan, M. J. Veit, C. J. Dorow, Y. Ge, Y. Li, W. Tabis, Y. Tang, X. Zhao, N. Barišić, and M. Greven, Phys. Rev. Lett. **113**, 177005 (2014).
[30] A. Narduzzo, A. Enayati-Rad, and S. Horii, N. E. Hussey, Phys. Rev. Lett. **98**, 146601 (2007).
[31] X. Xu *et al.*, J. Phys.: Condens. Matter **27**, 335701 (2015).
[32] A. Narayanan, M. D. Watson, S. F. Blake, N. Bruyant, L. Drigo, Y. L. Chen, D. Prabhakaran, B. Yan, C. Felser, T. Kong, P. C. Canfield, and A. I. Coldea, Phys. Rev. Lett. **114**, 117201 (2015).
[33] A. Kokalj, Comput. Mater. Sci. **28**, 155 (2003); J. Mol. Graphics Modell. **17**, 176 (1999); code available from http://www.xcrysden.org/.
[34] P. M. C. Rourke and S. R. Julian, Comput. Phys. Commun. **183**, 324 (2012).
[35] N. E. Alkseevskii and Yu. P. Gaidkov, Zh. Eksp. Teor. Fiz. **25**, 383 (1953).